Remote Sensing of Environment 198 (2017) 85–94

Contents lists available at ScienceDirect

Remote Sensing of Environment

journal homepage: www.elsevier.com/locate/rse

Sensing an intense phytoplankton bloom in the western Taiwan Strait from radiometric measurements on a UAV

Shaoling Shang [a,*], Zhongping Lee [b,*], Gong Lin [a], Chuanmin Hu [c], Lianghai Shi [a], Yongnian Zhang [d], Xueding Li [e], Jingyu Wu [f], Jing Yan [a]

[a] State Key Laboratory of Marine Environmental Science, Xiamen University, Xiamen 361005, China
[b] School for the Environment, University of Massachusetts Boston, Boston, MA 02125, USA
[c] College of Marine Science, University of South Florida, 140 Seventh Avenue, South, St. Petersburg, FL 33701, USA
[d] Fujian Institute of Surveying and Mapping, Fuzhou 350000, China
[e] Fujian Marine Forecast, Fuzhou 350000, China
[f] Key Laboratory of Underwater Acoustic Communication and Marine Information Technology (Xiamen University), Ministry of Education of China, Xiamen 361005, China

ARTICLE INFO

Article history:
Received 27 October 2016
Received in revised form 17 May 2017
Accepted 25 May 2017
Available online xxxx

Keywords:
Unmanned aerial vehicle
Remote sensing reflectance
Phytoplankton bloom

ABSTRACT

Rapid assessment of algal blooms in bays and estuaries has been difficult due to lack of timely shipboard measurements and lack of spatial resolution from current ocean color satellites. Airborne measurements may fill the gap, yet they are often hindered by the high cost and difficulty in deployment. Here we demonstrate the capacity of a low-cost, low-altitude unmanned aerial vehicle (UAV) in assessing an intense phytoplankton (*Phaeocystis globosa*) bloom (chlorophyll concentrations ranged from 7.3 to 45.6 mg/m^3) in the western Taiwan Strait. The UAV was equipped with a hyperspectral sensor to measure the water color with a footprint of 5 m at every 30 m distance along the flight track. A novel approach was developed to obtain remote sensing reflectance (R_{rs}) from the UAV at-sensor radiometric measurements. Compared with concurrent and co-located field measured R_{rs} (14 stations in total), the UAV-derived R_{rs} showed reasonable agreement with root mean square difference ranging 0.0028–0.0043 sr^{-1} (relative difference ~20–32%) of such turbid waters for the six MODIS bands (412–667 nm). The magnitude of the bloom was further evaluated from the UAV-derived R_{rs}. For the bloom waters, the estimated surface chlorophyll *a* concentration (*Chl*) ranged 6–98 mg/m^3, which is 3–50 times of the *Chl* under normal conditions. This effort demonstrates for the first time a successful retrieval of both water color (*i.e.*, R_{rs}) and *Chl* in a nearshore environment from UAV hyperspectral measurements, which advocates the use of UAVs for rapid assessment of water quality, especially for nearshore or difficult-to-reach waters, due to its flexibility, low cost, high spatial resolution, and sound accuracy.

1. Introduction

Phytoplankton blooms are natural phenomenon. Those blooms of particular note over decades, which adversely affect the health of ecosystems and human beings as well as the "health" of local and regional economies, are named harmful algal blooms (HABs) (Hallegraeff, 1993). Various techniques have been developed to help monitoring and early warning of HABs (Babin et al., 2005). Besides *in situ* observations, optical sensors onboard satellites were used to observe HABs and estimate concentrations of phytoplankton over broad regions – or generally termed as remote sensing approach. This technique is based on that there is a dramatic change of water color during these events due to significantly elevated phytoplankton concentrations, and a wide range of schemes have been developed for the utilization of satellite measurements (*e.g.*, Ahn and Shanmugam, 2006; Carder and Steward, 1985; Hu et al., 2005; Kurekin et al., 2014; Qi et al., 2016; Shang et al., 2014a; Sourisseau et al., 2016; Stumpf et al., 2003; Wynne et al., 2005). For instance, a chlorophyll anomaly technique that uses the increase in chlorophyll concentration of 1 mg/m^3 from the mean of the previous 60 days (Stumpf et al., 2003) was found very effective (>80%) for the detection of *Karenia brevis* blooms along the southwest Florida coast (Tomlinson et al., 2004). Based on field measurements of remote sensing reflectance and cell counts, the feasibility of using multispectral and hyperspectral approaches for detecting blooms of *Phaeocystis globosa* was assessed (Lubac et al., 2008). Using either total absorption or water-leaving reflectance field data, an algorithm was proposed to retrieve cell counts of *Phaeocystis* blooms in the southern North Sea waters (Astoreca et al., 2009). A novel floating algae index was developed, that employs the medium resolution (250 and 500 m) MODIS reflectance data at 645, 859, and 1240 nm, to identify locations of cyanobacteria blooms occurring in Taihu Lake, China (Hu et al., 2010). An HAB risk classification method, which employs a fully

* Corresponding authors.
E-mail addresses: slshang@xmu.edu.cn (S. Shang), ZhongPing.Lee@umb.edu (Z. Lee).

http://dx.doi.org/10.1016/j.rse.2017.05.036
0034-4257/

automatic data-driven approach to identify key characteristics of water leaving radiances and derived absorption and backscattering quantities, has obtained accurate results on MODIS and MERIS data, successfully identifying 89% of *Phaeocystis globosa* HABs in the southern North Sea and 88% of *Karenia mikimotoi* blooms in the Western English Channel (Kurekin et al., 2014). The hyperspectral imagery data collected onboard the International Space Station were found useful for evaluating the spatial variation of a ciliate bloom in western Long Island Sound (Dierssen et al., 2015). A fuzzy-method to distinguish two species of toxic dinoflagellates was developed based on satellite remote sensing reflectance and corresponding *in situ* record of species and cell counts, providing valuable information on the frequency and distribution of these HABs along the French continental shelf from 1998 to 2012 (Sourisseau et al., 2016).

Many HAB events occurring in coastal regions or inshore bays, however, are often patchy or with a small spatial coverage, and such events are many times unpredictable and fast changing. For ocean color satellites having a spatial resolution of 300 m or coarser and with a revisit time ~once per day (*e.g.*, MERIS, MODIS) or even lesser (*e.g.*, international space station), it is thus difficult to have reliable measurements of small-scale HAB blooms with such satellite sensors, especially due to the blocking effects of clouds. There are satellites having a much higher spatial resolution, such as Landsat (30 m) and Sentinel (10 m) designed basically for land observations, however, they have a revisit time of 5–16 days, thus they are far from satisfactory to meet an urgent need for monitoring a bloom event as well as continuous monitoring over days or even weeks. In addition, these sensors have wide spectral bands which are not feasible for an accurate assessment of bloom intensity. It is necessary to develop, and practice, new observational strategies to monitor such HAB events.

Unmanned aerial vehicles (UAVs), although originated mostly in military applications, have recently shown great value for environmental remote sensing, due to their flexibility and low cost, and very importantly, very high spatial resolution from the low flying height, to map details even under heavy clouds. The global UAV market revenue is worth 5.4 B€ as of 2013, and is expected to grow up to 6.4 B€ by 2018 (Colomina and Molina, 2014). So far, UAVs have been used mostly over land, carrying out centimeter-level qualitative monitoring with cameras, for example, to detect forest fire, vegetation, disaster damage on landscapes, and inshore aquaculture cages (*e.g.*, Berni et al., 2009; Laliberte and Rango, 2009, 2011; Lomax and Michelini, 2015; Martínez-de Dios et al., 2006; Rango et al., 2009; Turner et al., 2015; Yan et al., 2016). Recently photos taken from a UAV were used to help establish a 3-D observation of a nontoxic *Noctiluca scintillans* bloom event in the nearshore waters of the South China Sea (Xie et al., 2015). However, no reports have been found yet to quantitatively characterize phytoplankton bloom or HAB events based on radiometric measurements obtained from a UAV platform.

Here for the first time, we demonstrate a successful UAV assessment of a phytoplankton (*Phaeocystis globosa*) bloom in an estuary (Weitou Bay) in the western Taiwan Strait, where hyperspectral radiometers were mounted to measure the upward radiance and downward irradiance. The objective is two-fold: 1) to demonstrate the capacity of UAV in bloom assessment; 2) to develop a practical approach to quantitatively assess blooms from UAV radiometric measurements.

2. Background and *in situ* measurements

2.1. The phytoplankton bloom event

An intense phytoplankton bloom, dominated by *Phaeocystis globosa*, occurred in Weitou Bay during September 10 to 19, 2015 (Bulletin of Marine Environment of Fujian, 2015, the Fujian Marine Forecast). Weitou Bay is one of >10 bays and estuaries located in the western Taiwan Strait, where four medium- to small-size rivers discharge (see the red star symbol in Fig. 1a for the location of Weitou Bay). All these bays and estuaries are of high productivity, full of fishing and aquaculture activities.

According to the Bulletin of Marine Environment of Fujian, 2015, cell counts of *Phaeocystis globosa* were up to 200 gel matrix/L at the peak time of the bloom, and a rough estimate of the bloom area was ~150 km^2, covering the water from the outlet of Anhai Bay to Dabaiyu and then to Weitou Village (roughly the area circled by the grey line and the shoreline of the eastern Weitou Bay, see Fig. 1b). Note that one gel matrix is constituted by thousands of cells, and normally cell abundance $>10^6$ L^{-1} indicates presence of gel matrix or gelatinous colony forms (Schoemann et al., 2005).

A ship survey with UAV overflights was carried out in September 11–12, 2015 (Fig. 1b). The UAV flew mostly over the northeastern part of the bay only on September 12, 2015. The two-day ship survey comprised 18 stations with remote sensing reflectance (R_{rs}, sr^{-1}) measured *in situ* using a GER1500 spectroradiometer (Spectra Vista Corporation, USA), which covers a spectral range of 350–1050 nm with a spectral resolution of 3 nm. R_{rs} is defined as the ratio of water-leaving radiance (L_w) to downwelling irradiance just above the surface ($E_d(0+)$) (Mobley, 1994), and the R_{rs} spectrum contains information of water constituents and bottom if it is optically shallow. The method for R_{rs} data processing is detailed in Shang et al. (2011). Briefly, total reflectance (T_{rs}, sr^{-1}, ratio of total upwelling radiance to downwelling irradiance) and sky reflectance (S_{rs}, sr^{-1}, ratio of radiance from sky to downwelling irradiance) can be calculated from GER1500 measurements. R_{rs} is then obtained by deducting the reflected S_{rs} from T_{rs} and further removing of residual surface contribution (δ) through iterative derivations following Lee et al. (2010).

Water samples were also collected for fluorometric measurements of chlorophyll *a* concentration (*Chl*, mg/m^3) which were performed according to the Ocean Optics Protocol Version 2.0 (Mueller et al., 2002).

During the survey, the sky was clear and the sea state was calm. The water color of blooming waters was very different from that of non-bloom or "normal" water, as indicated in Fig. 1. Part of the water even turned reddish with visible phaeocystic gel matrix, for example, at Station Q7 (Fig. 1b). *In situ Chl* ranged from 7.3 to 45.6 mg/m^3, with higher concentration observed on September 12, 2015.

2.2. UAV surveys

In order to obtain a quantitative assessment of an HAB event using UAVs, *i.e.*, to provide an estimation of the bloom scale represented by concentrations of phytoplankton pigments (*e.g.*, chlorophyll *a*), the first step is to develop a method to obtain sound R_{rs} from radiometric measurements with the UAV platform. Note that unlike either ship-based measurement strategies (*e.g.*, Carder and Steward, 1985; Lee et al., 2013) or satellite-based measurement strategies (*e.g.*, Gordon et al., 1982), measurements *via* UAVs and associated data processing encountered different challenges, and no methods have yet reported in obtaining R_{rs} spectra from UAV measurements. To develop and test such a method, *in situ* measurements of R_{rs} with UAV overflights were carried out in Zhangjiang River estuary and Gulei Peninsula during 2014–2015 (see blue symbols in Fig. 1a for the location, and UAV flight tracks in Fig. 1c & d). During the surveys, the sky was mostly overcast or cloudy (see Table 1). A scheme to derive R_{rs} from UAV measurements is proposed and detailed below in Section 3.

3. Approach to derive R_{rs} from UAV measurements

3.1. Instrument and measurements

The UAV used in this study is an LT-150 (TOPRS Technology Co., Ltd., China) equipped with an AvaSpec-dual spectroradiometer (Avantes, Netherlands), which includes two sensors (see Fig. 2a) covering a spectral range of 360–1000 nm with a spectral resolution of 1 nm and a signal-to-noise ratio of ~100–400 in the visible domain. This spectroradiometer was factory calibrated. Two properties were measured with the two sensors: (1) total upwelling radiance ($L_t(h,\lambda,t)$, $W\,m^{-2}\,nm^{-1}\,sr^{-1}$), and (2) downwelling irradiance ($E_d(h,\lambda,t)$, $W\,m^{-2}\,nm^{-1}$), with h the altitude of

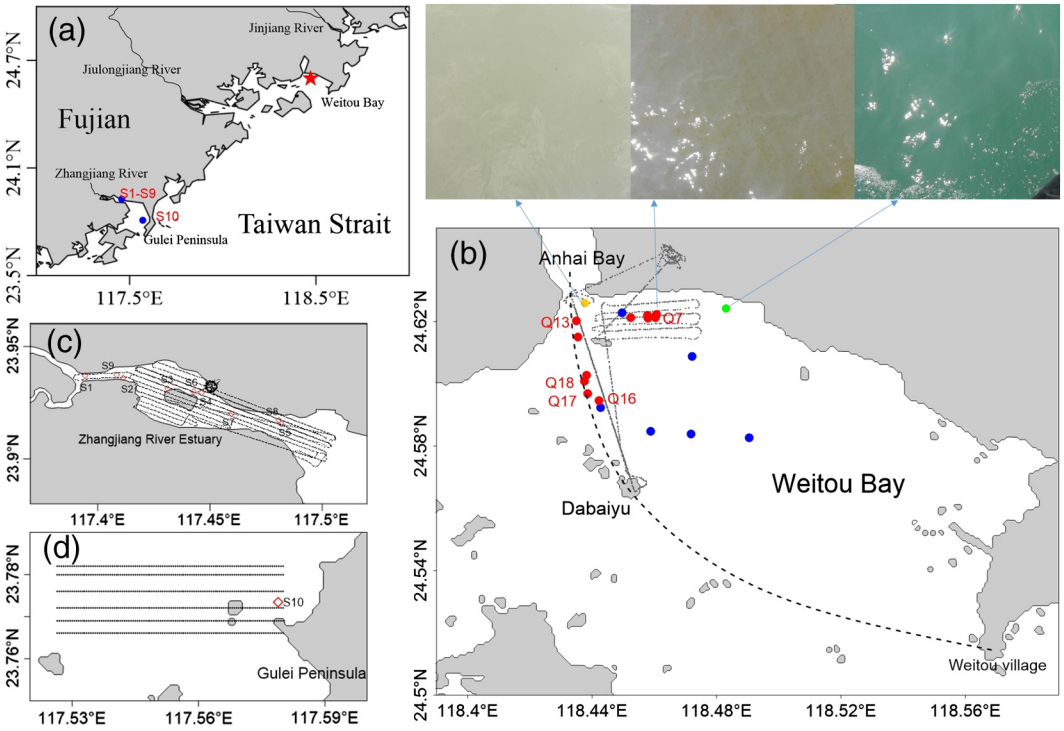

Fig. 1. (a) The Taiwan Strait; (b) the Weitou Bay, with its location shown as a red star in Fig. 1a; blue symbols show *in situ* sampling stations on September 11, 2015; survey on September 12, 2015 included *in situ* sampling (red symbols) and UAV flights (light dotted line); pictures were taken at Station Q7, also at two other contrasting sites (bloom water indicated by a yellow symbol and non-bloom water indicated by a green symbol); the dotted line extending from the outlet of Anhai Bay to Dabaiyu and then to Weitou Village shows a rough boundary of bloom area as reported by Fujian Marine Forecast; (c) *in situ* surveys (circles) with UAV overflights (light dotted line) in Zhangjiang River estuary, with its location shown as a blue symbol in Fig. 1a; (d) *in situ* surveys with UAV overflights in Gulei Peninsula, with its location shown as a blue symbol in Fig. 1a. (For interpretation of the references to color in this figure legend, the reader is referred to the web version of this article.)

the UAV and t the time when the measurements were taken. The current UAV-radiometer setup provides one line of data along the flight track, with a flying altitude of 300 m, which results in a surface pixel size of 5.2 m in diameter. The flying speed was 30 m/s, with a sampling rate of 1 Hz, which resulted in a ground resolution of 30 m (Fig. 2b). All UAV flights were carried out within the time frame of 9:00–16:30.

3.2. Derive R_{rs} from UAV

Because the sea surface is commonly roughened by waves, $L_t(h, \lambda, t)$ in general can be expressed as Lee et al. (2010):

$$L_t(h,\lambda,t) = L_{path}(\lambda,t) + \sum W(i) \times F(i) \times L_{sky}(\lambda,t,i) + T \times L_w(\lambda,t) \quad (1)$$

Here $L_{path}(\lambda,t)$ is the path radiance resulted from atmospheric scattering by the layer of atmosphere between the surface and the sensor at the UAV; $W(i) \times F(i) \times L_{sky}(\lambda,t,i)$ is the surface-reflected sky radiance with F the Fresnel reflectance corresponding to the observation of L_t and $W(i)$ for the weighting factor corresponding to $L_{sky}(\lambda,t,i)$ (Lee et al., 2010), while $L_{sky}(\lambda,t,i)$ is the downwelling sky radiance for facet i. T is the diffuse transmittance of the atmosphere and $L_w(\lambda,t)$ is the water leaving radiance. Note that unlike notations in many other publications

Table 1
Statistics for comparison between R_{rs} from UAV and matching up R_{rs} from GER at each station (400–750 nm).

Station number	Sea state[a]	Solar zenith angle [°]	Sky condition	Wind[b] speed (m/s)	RMSD	ε (%)	r
S1	1	33	Cloudy	1	0.0030	44	0.99
S2	1	29	Cloudy	1	0.0011	13	0.99
S3	1	25	Cloudy	1	0.0035	33	0.99
S4	2	22	Cloudy	1	0.0032	31	0.97
S5	3	19	Overcast	1	0.0031	26	0.96
S6	1	49	Overcast	1	0.0061	41	1.00
S7	2	52	Overcast	1	0.0081	57	0.99
S8	3	56	Overcast	1	0.0028	20	1.00
S9	1	49	Overcast	3	0.0024	14	0.99
S10	2	57	Clear	2	0.0027	14	1.00
Q13	1	52	Clear	5	0.0029	26	0.98
Q16	2	58	Clear	5	0.0017	11	0.97
Q17	2	59	Clear	5	0.0019	14	0.95
Q18	2	63	Clear	5	0.0029	22	0.95

[a] According to the standard released by the National Marine Forecast of China.
[b] The wind speed data is from https://rp5.ru/.

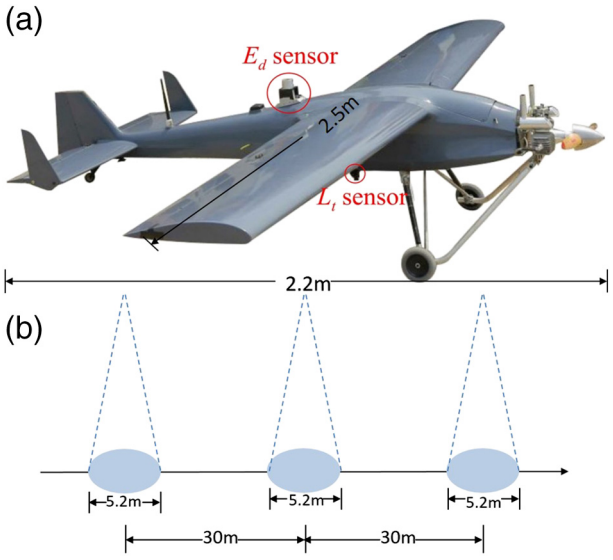

Fig. 2. (a) The LT-150 UAV equipped with the AvaSpec-dual sensor system (E_d to measure downwelling irradiance and L_t to measure upwelling radiance); (b) ground resolution along flight line.

for ocean color remote sensing, here L_{path} does not include the surface Fresnel reflected light because the latter is included explicitly in Eq. (1). Also, the effects of any likely white caps due to broken waves are included in the surface reflectance term.

In practice, because the flight altitude is just about 300 m, $L_{path}(\lambda,t)$ can be considered as negligible, and T is approximated as 1.0. Then Eq. (1) can be approximated to (Lee et al., 2010):

$$L_t(h,\lambda,t) = \overline{F} \times \overline{L_{sky}}(\lambda,t) + L_w(\lambda,t) + \delta(t) \times E_d(0+,\lambda,t) \quad (2)$$

where $\delta(t)$ is residual reflectance of the sea surface (due to white caps, *etc.*) in units of sr^{-1}, $\overline{F}$ is averaged F for all facets, and $\overline{L_{sky}}(\lambda,t)$ is averaged $W(i) \times L_{sky}(\lambda,t,i)$ for all facets. Considering that h is just 300 m, it is reasonable to approximate $E_d(h,\lambda,t)$ as the downwelling irradiance just above the water surface $E_d(0+,\lambda,t)$. Then dividing both sides of Eq. (2) by $E_d(0+,\lambda,t)$ results in:

$$T_{rs}(h,\lambda,t) = \overline{F} \times \overline{S_{rs}}(\lambda,t) + R_{rs}(\lambda,t) + \delta(t) \quad (3)$$

where T_{rs} is total reflectance and S_{rs} is sky reflectance. Because the radiance sensor looks down at nadir, $\overline{F}$ can be approximated to 0.023 (Mobley, 1994). R_{rs} is then derived as:

$$R_{rs}(\lambda,t) = T_{rs}(h,\lambda,t) - 0.023 \times \overline{S_{rs}}(\lambda,t) - \delta(t) \quad (4)$$

Then the key to derive R_{rs} from Eq. (4) is to estimate $\overline{S_{rs}}$ and δ, as detailed below.

3.2.1. Quality control on UAV raw data

Before R_{rs} can be derived from Eq. (4), quality control on raw data is imperative. This is because the measured $E_d(h,\lambda,t)$ and $L_t(h,\lambda,t)$ vary significantly due to tilts of the UAV platform as well as moving clouds. Here we used wavelet transform (Ebadi and Shafri, 2015) to filter out outliers in the measurements of $E_d(h,\lambda,t)$ and its corresponding $L_t(h,\lambda,t)$. Briefly,

(1) Use $E_d(h,\lambda,t)$ at 555 nm ($E_d(h,555,t)$) to determine measurements under stable UAV conditions. Specifically, implement wavelet transform for $E_d(h,555,t)$ to get smoothed $E_d(h,555,t)$ (hereafter s_$E_d(h,555,t)$); calculate relative difference between s_$E_d(h,555,t)$ and $E_d(h,555,t)$ for each flight line; retain those $E_d(h,555,t)$ that are within ±10% of s_$E_d(h,555,t)$, and retain those $E_d(h,\lambda,t)$ and $L_t(h,\lambda,t)$ corresponding to the selected $E_d(h,555,t)$. An example for such a processing, which was acquired under clear sky, is shown in Fig. 3, where only valid data (blue dots) after this quality control were used for further processing. Because of tilting of the UAV, there are clearly variations (within ±10% on average) of the resulted downwelling irradiance, which could contribute ±10% variation on the magnitude of remote sensing reflectance.

(2) Based on a visual examination and statistics, we found that data over land was featured by negative values for $T_{rs}(550)$–1.5 $T_{rs}(850)$. Thus we implemented an automatic procedure by calculating this value and discarding all measurements of E_d and L_t associated with a negative $T_{rs}(550)$–1.5 $T_{rs}(850)$.

After removing outliers in $E_d(h,\lambda,t)$ and $L_t(h,\lambda,t)$ as shown above, $L_t(h,\lambda,t)$ with potential serious sun glint were further examined following Kutser et al. (2009), *via* employing the O_2 absorption band at 760 nm. Specifically, the following was calculated for each L_t spectrum

$$G(t) = (L_t(h,755,t) + L_t(h,775,t))/2 - L_t(h,760,t) \quad (5)$$

If the difference between an individual $G(t)$ and the averaged G during a flight line is two times greater than the standard deviation of G within that flight line, the $L_t(h,\lambda,t)$ associated with this $G(t)$ as well as its corresponding $E_d(h,\lambda,t)$ were discarded; otherwise the $L_t(h,\lambda,t)$ data for this line were retained as valid data and used subsequently for the derivation of R_{rs}. It is noteworthy that no serious sun glint was detected in all our UAV dataset after the two-step quality control for removing outliers (*i.e.*, implementing wavelet transform and then removing land data).

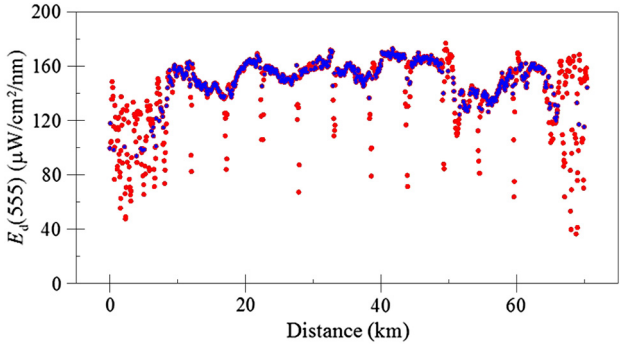

Fig. 3. An example of $E_d(h,555,t)$ before and after wavelet transform; red: discarded data; blue: valid data after wavelet transform. (For interpretation of the references to color in this figure legend, the reader is referred to the web version of this article.)

3.2.2. Removing $\overline{S_{rs}}$ and residual reflectance δ

After L_t and E_d were determined, T_{rs} was calculated as a simple ratio of L_t to E_d. It then requires to remove $\overline{S_{rs}}$ and residual reflectance δ before R_{rs} can be derived from Eq. (4).

However, there was no sensor on the UAV to measure L_{sky} during the UAV flights. Here we simply implemented the bio-optical model and the iterative approach of Lee et al. (2010) to estimate and remove $\overline{S_{rs}}$ and δ, with $S_{rs}(500)$ included as an extra variable in the optimization procedure, and taking usage of the spectral dependence of $S_{rs}(\lambda)$ as shown below.

Following Toole et al. (2000) and Gould et al. (2001), the spectral dependence of $S_{rs}(\lambda)$ can be expressed as:

$$S_{rs}(\lambda) = S_{rs}(500) \times e^{-k(\lambda-500)} \quad (6)$$

An *in situ* dataset (n = 60) measured by our group using a GER1500 fits Eq. (6) well (Fig. 4a), and it was also found from this dataset that the slope k was significantly correlated with $S_{rs}(500)$ (see Fig. 4b), with

$$k = 0.0079 \times e^{-8.488 \times S_{rs}(500)} \quad (7)$$

Note that lower $S_{rs}(500)$ corresponds to higher k, meaning that the sky reflectance is more blue-rich.

4. Results

4.1. R_{rs} from UAV compared to R_{rs} from GER

Based on the above processes, $R_{rs}(\lambda,t)$ can be derived from $L_t(h,\lambda,t)$ and $E_d(h,\lambda,t)$ measured onboard the UAV (represented as $R_{rs}(\lambda,t)$_u or R_{rs}_u). To evaluate the quality of $R_{rs}(\lambda,t)$_u, a comparison between $R_{rs}(\lambda,t)$_u and concurrent ship-borne (*i.e.*, field measured) R_{rs} (represented as R_{rs}_f) using a GER1500 was carried out. When matching up $R_{rs}(\lambda,t)$_u with the R_{rs}_f, to ensure a larger number of match-ups for statistical analysis, we used measurements co-located to within 500 m spatially and within 30 min temporally. A total of 10 match-ups were compiled (see symbols in Fig. 1c & d for the location of these 10 stations). In addition, following community-accepted practices (*e.g.*, Hooker et al., 2002; Lee and Hu, 2006; Mélin et al., 2007; Moore et al., 2009), the root mean square difference (RMSD) and averaged unbiased absolute percentage difference (ε), as well as the correlation coefficient

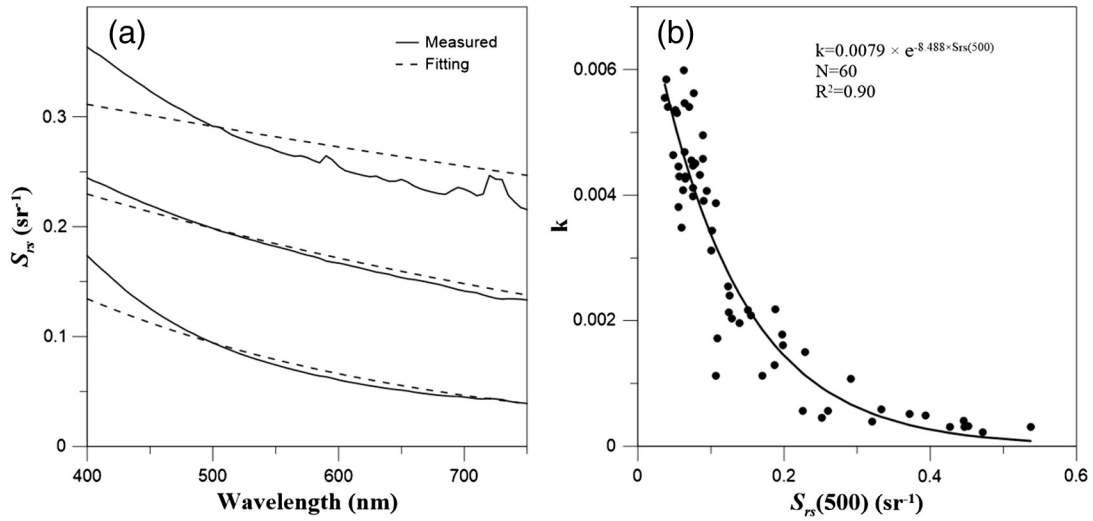

Fig. 4. (a) Spectral dependence of $S_{rs}(\lambda)$ at a range of 400 nm to 750 nm; dashed line: $S_{rs}(\lambda)$ calculated based on Eqs. (6)–(7), using $S_{rs}(500)$ of ~0.1 sr^{-1}, 0.2 sr^{-1} and 0.3 sr^{-1}; solid curve: measured $S_{rs}(\lambda)$; (b) $S_{rs}(500)$ *vs* k, where k is the spectral slope of sky reflectance defined in Eq. (7).

(r) in linear regression analysis, were used to measure the consistency between field measured (f) and UAV determined (u) datasets:

$$\varepsilon = \left[\frac{1}{n}\sum_{i=1}^{n}\frac{|u_i - f_i|}{u_i + f_i}\right] \times 200\% \quad (8)$$

$$\mathrm{RMSD} = \sqrt{\frac{1}{n}\sum_{i=1}^{n}[(u_i)-(f_i)]^2} \quad (9)$$

Here n is the total number of data points.

The comparison of the 10 match-ups suggests that these two measurements are highly consistent with each other. As an example, Fig. 5a shows R_{rs} spectrum (400–750 nm) of two stations, where consistent spectrum of R_{rs}_u and R_{rs}_f are observed. A novel quality assurance (QA) system (Wei et al., 2016) was also used to evaluate the quality of R_{rs}_u for the 10 stations (Fig. 5b). In 8 out of 10 stations, R_{rs}_u had scores >0.8, demonstrating high quality of these R_{rs}_u. Statistics for the comparison between these 10 R_{rs}_u and R_{rs}_f match-ups are also summarized in Table 2.

Statistically the unbiased absolute percentage difference (ε) is in a range of ~22–41% (with a mean value as ~27%) at the six MODIS ocean-color bands (412–667 nm), with RMSD ranging ~0.0032–0.0048 sr^{-1}. These differences, however, could be a result of factors and components associated with the determination of both R_{rs}_u and R_{rs}_f. For instance, the values of both R_{rs}_f and R_{rs}_u depend on the calibration of sensors used in the measurements. The higher ε (then lower RMSD) value is at 412 nm, where $R_{rs}(412)$ is very low, is likely due to strong contribution of CDOM for such estuary water body. These statistics measures are actually similar to the evaluation results when comparing satellite products with *in situ* measurements for coastal turbid waters (Zibordi et al., 2009). These values, however, are slightly higher than those found between MODIS and *in situ* measurements for the western Taiwan Strait (Dong, 2010), and between MODIS and *in situ* measurements for the northeastern South China Sea and the Taiwan Strait (a combination of both oligotrophic waters and turbid nearshore waters, Shang et al. (2014b)). This slightly higher uncertainty in R_{rs} evaluation than that in previous studies is a result of 1) smaller number (just 10 stations here) of match-up analysis, and 2) these stations are located in more turbid waters of the western Taiwan Strait (Zhangjiang River estuary and Gulei Peninsula, see Fig. 1c & d). Therefore, considering the turbid and patchy nature of the water environment and the difficulty in UAV data processing, these uncertainties are considered as reasonable. Nevertheless, these differences in R_{rs} magnitude, which are

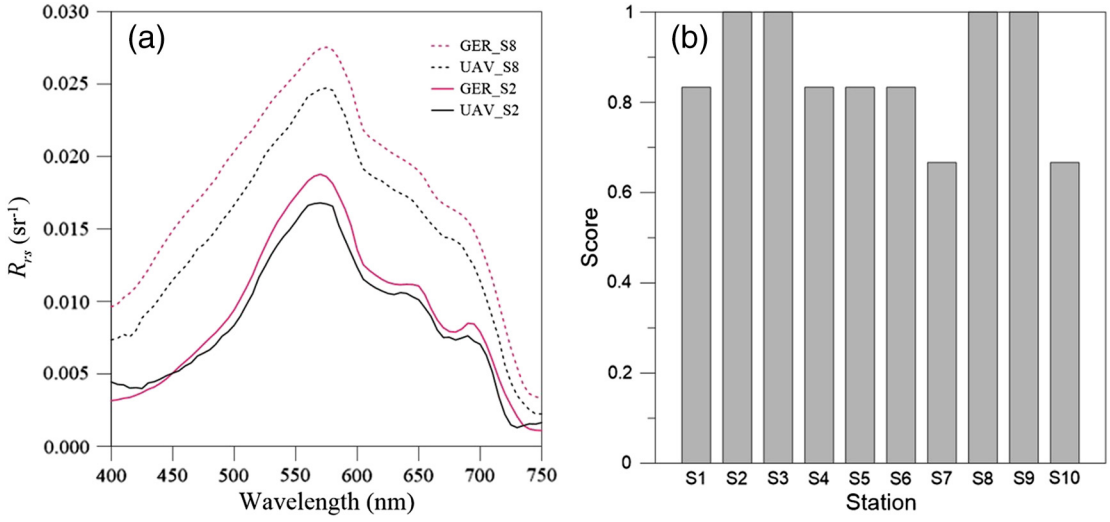

Fig. 5. (a) R_{rs}_u compared to concurrent R_{rs}_f; data of two stations (S2, solid; S8, dashed) are shown as examples; (b) scores of the R_{rs}_u of Stations S1–S10 evaluated by a quality assurance system (Wei et al., 2016).

Table 2
Statistics for comparison between R_{rs} from UAV and matching up R_{rs} from GER at six bands of MODIS.

MODIS bands (nm)[a]	412	443	488	531	547	667
RMSD	0.0032	0.0038	0.0045	0.0048	0.0048	0.0038
ε (%)	41	36	30	24	22	22
r	0.49	0.66	0.72	0.62	0.60	0.82
MODIS bands (nm)[b]	412	443	488	531	547	667
RMSD	0.0028	0.0033	0.0040	0.0042	0.0043	0.0035
ε (%)	32	32	27	21	20	22
r	0.50	0.65	0.69	0.60	0.54	0.78

[a] These MODIS statistics only included the 10 match-ups (Stations S1–S10).
[b] These MODIS statistics included Weitou Bay match-ups (14 in total).

actually not significant, will have more impact on the retrieval of the backscattering coefficient rather than the absorption coefficient, as it is the former that depends more on the magnitude of R_{rs}.

4.2. The bloom in Weitou Bay observed with the UAV

With confidence in the derived R_{rs} from our UAV measurements, we take advantage of the UAV system to sense the *Phaeocystis* bloom in Weitou Bay as described in Section 2.1. The UAV flew over the eastern Weitou Bay during 15:56–16:29 on September 12, 2015, while *in situ* measurements were carried out simultaneously. Likely due to the stronger wind condition on this day (see Table 1), apparently the UAV was tilted which resulted in a ~30% under-measurements in E_d when compared to that estimated by RADTRAN (Gregg and Carder, 1990). We therefore scaled the UAV-measured $E_d(h, \lambda, t)$ during this overflight by 1.3 in the process of calculating R_{rs}_u.

There were four *in situ* stations, Stations Q13, Q16, Q17 and Q18, that were within 500 m and 30 min of the UAV overflight (see Fig. 1b for the location). Again, R_{rs}_u derived from the UAV measurements are quite consistent with R_{rs}_f for these four Stations (see Fig. 6a). The ε values are in a range of ~11–26% (with a mean value as ~18%), with RMSD values in a range of 0.0017–0.0029 sr^{-1} and excellent correlations ($r > 0.95$) (see Table 1). These comparisons further confirm that our data collection and processing system with an UAV platform is valid.

Fig. 6b presents all the derived R_{rs}_u for UAV overflights on September 12, 2015, while examples of R_{rs}_u with distinct strong peaks around 700 nm (red curves) and peaks around 683 nm (black curves) are highlighted in Fig. 6c. The peak around 700 nm is a clear indicator of waters with intense phytoplankton bloom as often observed from *in situ* measurements (*e.g.*, Dierssen et al., 2006; Gitelson, 1992). In addition, 74% of all the derived R_{rs}_u show QA scores (Wei et al., 2016) >0.8, which further indicates satisfied quality of these R_{rs}_u spectra (Fig. 6d).

R_{rs}_u data were then used for *Chl* estimation using an empirical algorithm (shown below) developed for phytoplankton bloom waters alongshore the western Taiwan Strait based on a wavelength-shift algorithm (Gitelson, 1992) and a fluorescence line height (FLH) algorithm (Letelier and Abbott, 1996).

When the wavelength of maximum R_{rs} in the range of 677 nm to 715 nm (λ_{max}) is >692 nm, we have

$$Chl = 6.65 \times \lambda_{max} - 4569.10 \quad (10)$$

Otherwise FLH is calculated, which is further converted to *Chl*:

$$\mathrm{FLH} = R_{rs}(681) - R_{rs}(665) - 0.2 \times [R_{rs}(745) - R_{rs}(665)] \quad (11)$$

$$Chl = 9498.90 \times \mathrm{FLH} - 0.42 \quad (12)$$

The coefficients of these empirical algorithms were tuned based on a separate hyperspectral dataset of our group collected in the western Taiwan Strait (unpublished data; see Appendix).

The resulted *Chl* products are shown in Fig. 7. Higher *Chl* values in the northeastern Weitou Bay were found, which was also found in the limited *in situ* measurements on the same day (*i.e.*, September 12, 2015, also see circles overlaid in Fig. 7). Specifically, the estimated *Chl* from the UAV measurements at Stations Q13, Q16, Q17 and Q18 was 13.8 mg/m^3, 16.6 mg/m^3, 17.3 mg/m^3 and 16.6 mg/m^3 respectively, while the corresponding *in situ* values were 15.4 mg/m^3, 14.8 mg/m^3, 14.4 and 16.6 mg/m^3. Based on these four limited match-ups, the difference between UAV estimates and the *in situ* measurements was <20%. This deviation between UAV sensed *Chl* and *in situ Chl* is much lower than in the Taiwan Strait between MODIS *Chl* and its *in situ* match-ups, of which the average percentage error is 136% (Shang et al., 2011). Note that Weitou Bay is one of the inner bays in the western Taiwan Strait (see Fig. 1 for its location).

Normally in Weitou Bay in early fall, *Chl* is <2.0 mg/m^3 (personal communication with Mr. Dewen Chen at SOA Marine Forecast of Xiamen). The estimated *Chl* from the UAV measurements ranged 6–98 mg/m^3, suggesting a 3–50 fold increase in the chlorophyll concentration due to this phytoplankton bloom. Furthermore, the bloom covered almost the entire UAV tracks, with the most intense bloom close to the northeastern shore of Weitou Bay (the circled zone in Fig. 7).

5. Discussion

5.1. UAV data reduction

One of the major challenges in airborne remote sensing of coastal water environments is to obtain accurate R_{rs} from at-sensor calibrated radiance. This is because: (1) most available atmospheric correction to remove path radiance has been designed for satellite use where look-up tables (LUTs) were constructed at the top-of-atmosphere (TOA) level while airborne flights are often at much lower altitude (300 m in this study); (2) most commercially available atmospheric correction modules (*e.g.*, ENVI FLAASH) are designed for land use, where the Fresnel reflectance of the water surface is regarded as part of the to-be-retrieved surface reflectance instead of part of path radiance (Hu and Carder, 2002), leading to errors in the retrieved R_{rs}.

Most atmospheric correction of airborne hyperspectral measurements require tedious pre-processing to establish sensor-specific LUTs suitable for the sensor altitude (Gao et al., 2007; Zhang et al., 2015) or image-specific manual processing to take advantage of cloud shadows (Lee et al., 2007). In this study, due to the low-altitude (300 m) flights, neither is available or necessary. Rather, a practical approach, similar to the approach for data reduction of ship-based measurements but with consideration of sky color and residual errors in Fresnel reflection removal, has been developed and proven effective in deriving R_{rs}. Although the approach has not been tested elsewhere, we believe that the principles and the general assumptions should hold for other low-altitude cases, especially when considering that all data used in this study was collected in turbid bays and estuaries, and 9 out of 10 match-ups of UAV and *in situ* measurements were obtained in cloudy/overcast weather (see Table 1). On the other hand, for higher-altitude flights (*e.g.*, >1 km), the same approach may lead to larger errors because the path radiance term in Eq. (4) can no longer be neglected. Under those circumstances, more sophisticated approaches are required for effective atmospheric correction.

5.2. UAVs for coastal water monitoring

Estuaries and bays are places where HABs often occur. For their small sizes and proximity to land, the use of UAVs is a good option to meet urgent needs of event response. In this study, it took a UAV team roughly 30 min to get the system ready for the flight. In addition, compared to manned aircrafts that often fly over 1-km altitude (*e.g.*, Zhang et al., 2015), the low-altitude (several hundred meters) flight of UAVs not only obtains a zoom-in observation of the events, but also makes it

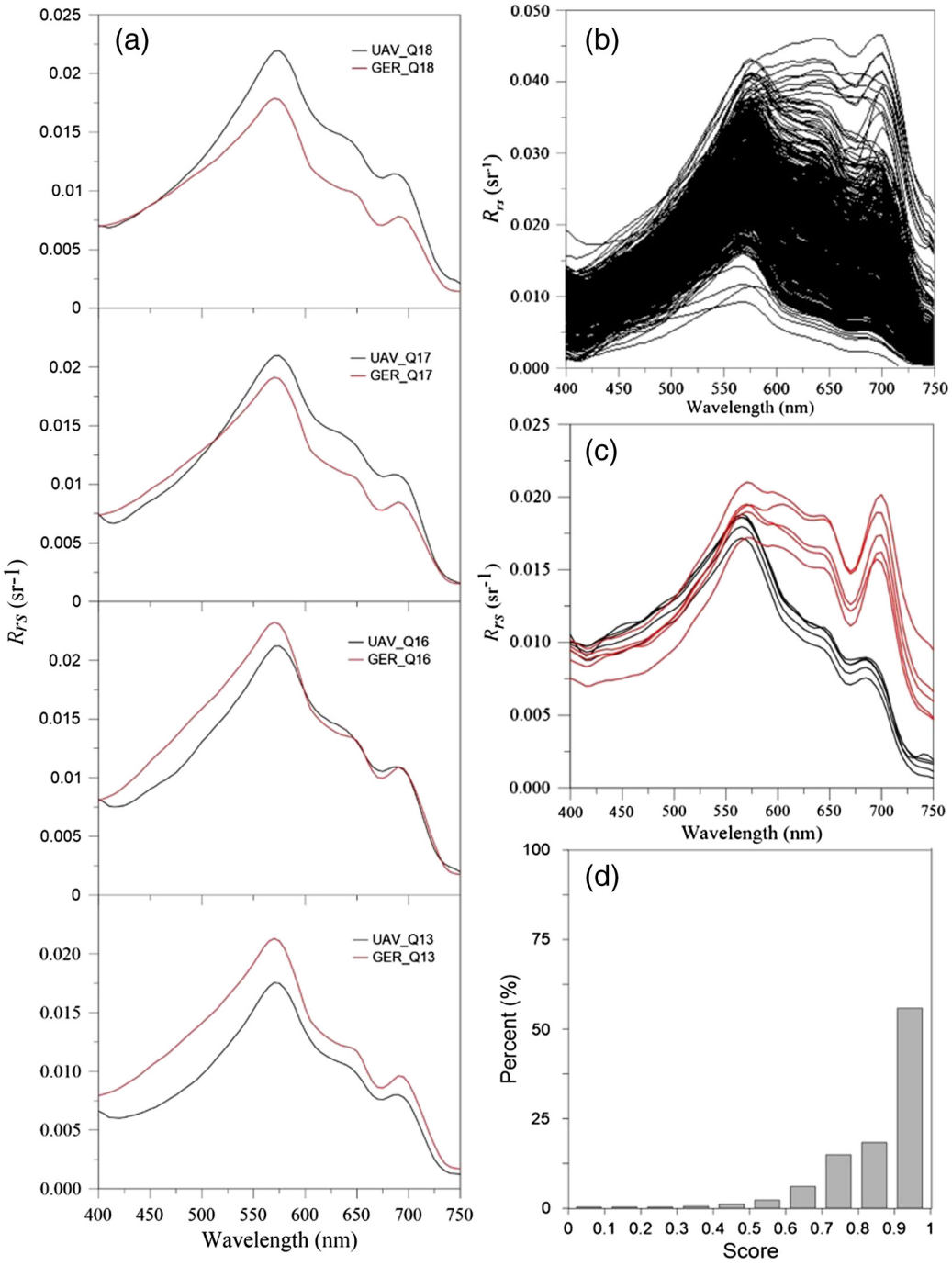

Fig. 6. (a) R_{rs}_u compared to concurrent R_{rs}_f measured in Weitou Bay (4 match-ups available); (b) all R_{rs}_u collected over Weitou Bay (n = 697); (c) examples of R_{rs}_u showing strong peaks around 700 nm (red curves) compared to R_{rs}_u with peaks around 683 nm (black curves); (d) frequency distribution of scores of all R_{rs}_u evaluated by a quality assurance system (Wei et al., 2016). (For interpretation of the references to color in this figure legend, the reader is referred to the web version of this article.)

easier for data reduction as less atmosphere is between the sensor and the target, leading to possibly higher quality of R_{rs} spectra and quicker data turn-around for event response.

Similar to sensors mounted on manned aircrafts, hyperspectral measurements from UAVs have higher spatial and spectral resolutions than most satellite measurements, where the latter are often inadequate to assess blooms or other features in nearshore waters. For example, the distribution and magnitude of the bloom in Weitou Bay cannot be revealed by MODIS images at either 1-km or 500-m resolution or by Landsat 8 image at 30-m resolution. This is demonstrated in Fig. 8, where Fig. 8a shows a MODIS *Chl* image (1-km resolution) on September 12, 2015 after relaxing several flags (HILT and CLOUD) to enable sufficient data coverage; and Fig. 8b shows a MODIS color index (CI) image (500-m resolution) on the same day processed following Hu (2011). Fig. 8c shows a Landsat 8 true color image (30-m resolution) on September 11, 2015. While MODIS *Chl* image revealed relatively high *Chl* in nearshore waters in the northeastern Weitou Bay, it lacks resolution to show detailed spatial features. The same problem was found for the MODIS CI image even though its spatial resolution is higher. The Landsat 8 image (Fig. 8c) provides more detailed spatial features but no clear pattern of the bloom (the bloom covered the area east to the red line in Fig. 8c, as reported by the Fujian Marine Forecast). This is likely due to the wide and limited spectral bands of Landsat sensors that diminish the important spectral signatures of phytoplankton (see Fig. 8d).

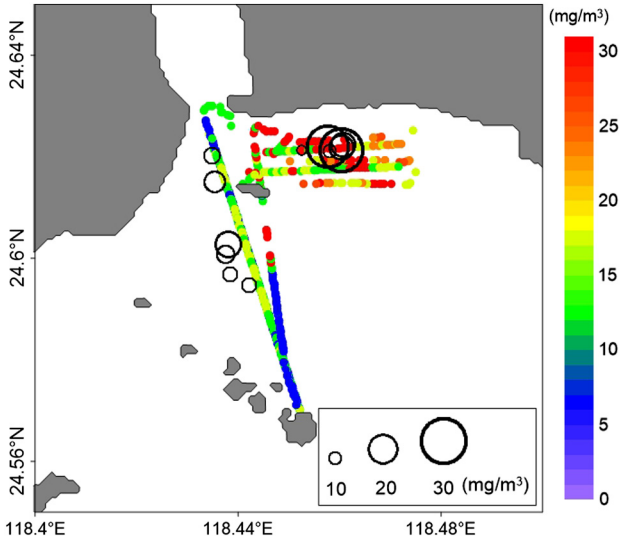

Fig. 7. *Chl* estimated from the UAV measurements on September 12, 2015, with black circles representing measurements from water sample analysis. The UAV measurements took place between 15:56 and 16:29.

Clearly, for small and patchy targets such as phytoplankton blooms in nearshore waters, UAVs equipped with hyperspectral sensors are viable systems to quickly capture fine spatial details in responding to such dynamic events. However, as always a high-spatial resolution system will lack a spatial coverage. This shortcoming could be addressed with multiple UAVs and/or extended overflights. Further, unlike satellite measurements where data processing is more or less standardized, hyperspectral UAV flights and associated data processing are still at its infancy. It will take dedicated efforts before unified protocols are established. Nevertheless, given the easiness and low cost to operate a UAV, we expect to see more measurements and data processing schemes in the near future to advance the UAV platform for aquatic remote sensing.

Coastal environments are highly dynamic due to tidal influence, wind stressing, or physical/biological aggregation, therefore often requiring more frequent measurements than that provided by typical polar-orbiting satellites (Lou and Hu, 2014). Without a geostationary satellite, UAVs may provide repeated high spatial resolution measurements of the same locations to examine the bloom dynamics; this is in addition to assessing the bloom magnitude and extent. While manned airborne measurements have been demonstrated to be capable of studying short-term changes in coastal environments (*e.g.*, Zhang et al., 2016), the use of UAVs, which are more flexible for low-altitude

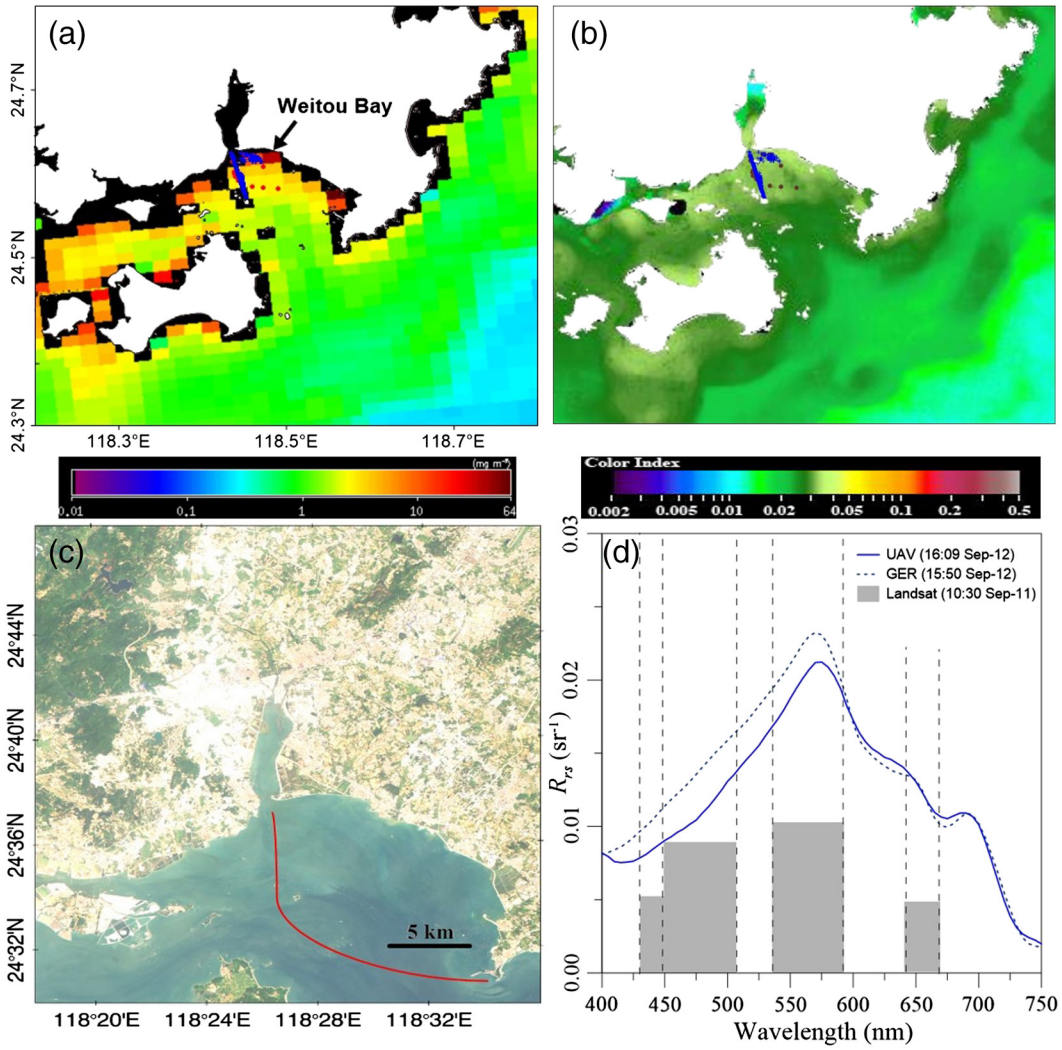

Fig. 8. MODIS *Chl* (a) and color index; (b) images on September 12, 2015 over Weitou Bay and its adjacent waters, overlaid with the locations of UAV (blue) and *in situ* (red) measurements; (c) Landsat 8 true color image on September 11, 2015 over Weitou Bay, with the red line indicating boundary of the *Phaeocystis* bloom; (d) Landsat 8 R_{rs} (grey bar, processed using ACOLITE with SWIR atmospheric correction (Vanhellemont and Ruddick, 2015)) compared to R_{rs} from UAV (solid line) and GER (dashed line) at Station Q16. (For interpretation of the references to color in this figure legend, the reader is referred to the web version of this article.)

repeated deployments, is at its infancy for the same purpose, thus requiring more research.

6. Conclusions

Although data is limited, this case study proved for the first time that it is possible to derive sound R_{rs} spectra from radiometric measurements taken on a UAV. This is also the first time that fine-resolution spatial distribution and magnitude of a phytoplankton bloom were obtained from the same UAV measurement in a small region. Such fine-resolution measurements with rapid response to HAB events are difficult with conventional ocean color satellites or manned aircrafts. These results support the deployment of such systems in a routine manner during bloom seasons, where the timely information on bloom magnitude, extent and evolution may aid the study of bloom mechanism and management decisions through providing key observations. However, the UAV system and the data processing protocols are far from mature, more efforts are necessary to improve the measurement system and refine the processing schemes in order to take a full advantage of such flexible and agile systems for routine monitoring of aquatic environments.

Acknowledgements

This study was jointly supported by the NSF-China (#41576169) and the Chinese Ministry of Science and Technology (#2016YFC1400905, #2016YFA0601201, #2016YFC1400906), the Programme of Introducing Talents of Discipline to Universities (#B07034), and the University of Massachusetts Boston. We thank Mr. Yujie Shan and Mr. Yue Gao for participating in *in situ* measurements.

Appendix A. Supplementary data

Supplementary data to this article can be found online at http://dx.doi.org/10.1016/j.rse.2017.05.036.

References

Ahn, Y.-H., Shanmugam, P., 2006. Detecting the red tide algal blooms from satellite ocean color observations in optically complex Northeast-Asia coastal waters. Remote Sens. Environ. 103, 419–437.
Astoreca, R., Rousseau, V., Ruddick, K., Knechciak, C., Van Mol, B., Parent, J.-Y., Lancelot, C., 2009. Development and application of an algorithm for detecting *Phaeocystis globosa* blooms in the case 2 southern North Sea waters. J. Plankton Res. 31, 287–300.
Babin, M., Cullen, J., Roesler, C., Donaghay, P., Doucette, G., Kahru, M., Lewis, M., Scholin, C., Sieracki, M., Sosik, H., 2005. New approaches and technologies for observing harmful algal blooms. Oceanography 18, 210–227.
Berni, J.A., Zarco-Tejada, P.J., Suárez, L., Fereres, E., 2009. Thermal and narrowband multispectral remote sensing for vegetation monitoring from an unmanned aerial vehicle. IEEE Trans. Geosci. Remote Sens. 47, 722–738.
Carder, K., Steward, R., 1985. A remote-sensing reflectance model of a red-tide dinoflagellate off West Florida. Limnol. Oceanogr. 30, 286–298.
Colomina, I., Molina, P., 2014. Unmanned aerial systems for photogrammetry and remote sensing: a review. ISPRS J. Photogramm. Remote Sens. 92, 79–97.
Dierssen, H., Kudela, R., Ryan, J., Zimmerman, R., 2006. Red and black tides: quantitative analysis of water-leaving radiance and perceived color for phytoplankton, colored dissolved organic matter, and suspended sediments. Limnol. Oceanogr. 51, 2646–2659.
Dierssen, H., McManus, G., Chlus, A., Qiu, D., Gao, B.-C., Lin, S., 2015. Space station image captures a red tide ciliate bloom at high spectral and spatial resolution. Proc. Natl. Acad. Sci. 112, 14783–14787.
Dong, Q., 2010. Studies on Remote Sensing of Phytoplankton Based on Absorption Properties and Its Application [D]. Xiamen University, In.
Ebadi, L., Shafri, H., 2015. A stable and accurate wavelet-based method for noise reduction from hyperspectral vegetation spectrum. Earth Sci. Inf. 8, 411–425.
Fujian Marine Forecast, 2015. Bulletin of Marine Environment of Fujian. http://www.fjmf.gov.cn/RedTide/RedTide.aspx (Chinese).
Gao, B., Montes, M., Li, R., Dierssen, H.M., Davis, C., 2007. An atmospheric correction algorithm for remote sensing of bright coastal waters using MODIS land and ocean channels in the solar spectral region. IEEE Trans. Geosci. Remote Sens. 45, 1835–1843.
Gitelson, A., 1992. The peak near 700 nm on radiance spectra of algae and water: relationships of its magnitude and position with chlorophyll concentration. Int. J. Remote Sens. 13, 3367–3373.
Gordon, H., Clark, D., Brown, J., Brown, O., Evans, R., 1982. Satellite measurement of the phytoplankton pigment concentration in the surface waters of a warm core gulf stream ring. J. Mar. Res. 40, 491–502.
Gould, R., Arnone, R., Sydor, M., 2001. Absorption, scattering, and, remote-sensing reflectance relationships in coastal waters: testing a new inversion algorithm. J. Coast. Res. 328–341.
Gregg, W.W., Carder, K.L., 1990. A simple spectral solar irradiance model for cloudless maritime atmospheres. Limnol. Oceanogr. 35, 1657–1675.
Hallegraeff, G., 1993. A review of harmful algal blooms and their apparent global increase. Phycologia 32, 79–99.
Hooker, S., Lazin, G., Zibordi, G., McLean, S., 2002. An evaluation of above-and in-water methods for determining water-leaving radiances. J. Atmos. Ocean. Technol. 19, 486–515.
Hu, C., 2011. An empirical approach to derive MODIS ocean color patterns under severe sun glint. Geophys. Res. Lett. 38, L01603.
Hu, C., Carder, K.L., 2002. Atmospheric correction for airborne sensors: comment on a scheme used for CASI. Remote Sens. Environ. 79, 134–137.
Hu, C., Muller-Karger, F., Taylor, C., Carder, K., Kelble, C., Johns, E., Heil, C., 2005. Red tide detection and tracing using MODIS fluorescence data: a regional example in SW Florida coastal waters. Remote Sens. Environ. 97, 311–321.
Hu, C., Lee, Z., Ma, R., Yu, K., Li, D., Shang, S., 2010. Moderate resolution imaging spectroradiometer (MODIS) observations of cyanobacteria blooms in Taihu Lake, China. J. Geophys. Res. 115, C04002.
Kurekin, A., Miller, P., Van der Woerd, H., 2014. Satellite discrimination of *Karenia mikimotoi* and *Phaeocystis* harmful algal blooms in European coastal waters: merged classification of ocean colour data. Harmful Algae 31, 163–176.
Kutser, T., Vahtmäe, E., Praks, J., 2009. A sun glint correction method for hyperspectral imagery containing areas with non-negligible water leaving NIR signal. Remote Sens. Environ. 113, 2267–2274.
Laliberte, A.S., Rango, A., 2009. Texture and scale in object-based analysis of subdecimeter resolution unmanned aerial vehicle (UAV) imagery. IEEE Trans. Geosci. Remote Sens. 47, 761–770.
Laliberte, A.S., Rango, A., 2011. Image processing and classification procedures for analysis of sub-decimeter imagery acquired with an unmanned aircraft over arid rangelands. GIScience & Remote Sensing 48, 4–23.
Lee, Z., Hu, C., 2006. Global distribution of case-1 waters: an analysis from SeaWiFS measurements. Remote Sens. Environ. 101, 270–276.
Lee, Z., Casey, B., Arnone, R., Weidemann, A., Parsons, R., Montes, M., Gao, B.-C., Goode, W., Davis, C., Dye, J., 2007. Water and bottom properties of a coastal environment derived from Hyperion data measured from the EO-1 spacecraft platform. J. Appl. Remote. Sens. 1, 011502–011516.
Lee, Z., Ahn, Y.-H., Mobley, C., Arnone, R., 2010. Removal of surface-reflected light for the measurement of remote-sensing reflectance from an above-surface platform. Opt. Express 18, 26313–26324.
Lee, Z., Pahlevan, N., Ahn, Y.-H., Greb, S., O'Donnell, D., 2013. Robust approach to directly measuring water-leaving radiance in the field. Appl. Opt. 52, 1693–1701.
Letelier, R.M., Abbott, M.R., 1996. An analysis of chlorophyll fluorescence algorithms for the moderate resolution imaging spectrometer (MODIS). Remote Sens. Environ. 58, 215–223.
Lomax, A., Michelini, A., 2015. Rapid determination of earthquake size for hazard warning. J. Geol. Soc. India 66, 365–366.
Lou, X., Hu, C., 2014. Diurnal changes of a harmful algal bloom in the East China Sea: observations from GOCI. Remote Sens. Environ. 140, 562–572.
Lubac, B., Loisel, H., Guiselin, N., Astoreca, R., Felipe Artigas, L., Mériaux, X., 2008. Hyperspectral and multispectral ocean color inversions to detect *Phaeocystis globosa* blooms in coastal waters. J. Geophys. Res. 113, C06026.
Martínez-de Dios, J., Merino, L., Caballero, F., Ollero, A., Viegas, D., 2006. Experimental results of automatic fire detection and monitoring with UAVs. For. Ecol. Manag. 234, S232.
Mélin, F., Zibordi, G., Berthon, J.-F., 2007. Assessment of satellite ocean color products at a coastal site. Remote Sens. Environ. 110, 192–215.
Mobley, C.D., 1994. Light and Water: Radiative Transfer in Natural Waters. Academic press.
Moore, T.S., Campbell, J.W., Dowell, M.D., 2009. A class-based approach to characterizing and mapping the uncertainty of the MODIS ocean chlorophyll product. Remote Sens. Environ. 113, 2424–2430.
Mueller, J., Mueller, J., Pietras, C., Hooker, S., Clark, D., Frouin, A.M.R., Mitchell, B., Bidigare, R., Trees, C., Werdell, J., 2002. Ocean optics protocols for satellite ocean color sensor validation, revision 3, volumes 1 and 2. NASA Tech. Memo. 210004.
Qi, L., Hu, C., Xing, Q., Shang, S., 2016. Long-term trend of *Ulva prolifera* blooms in the western Yellow Sea. Harmful Algae 58, 35–44.
Rango, A., Laliberte, A., Herrick, J., Winters, C., Havstad, K., Steele, C., Browning, D., 2009. Unmanned aerial vehicle-based remote sensing for rangeland assessment, monitoring, and management. J. Appl. Remote. Sens. 3, 033542.
Schoemann, V., Becquevort, S., Stefels, J., Rousseau, V., Lancelot, C., 2005. *Phaeocystis* blooms in the global ocean and their controlling mechanisms: a review. J. Sea Res. 53, 43–66.
Shang, S., Dong, Q., Lee, Z., Li, Y., Xie, Y., Behrenfeld, M., 2011. MODIS observed phytoplankton dynamics in the Taiwan Strait: an absorption-based analysis. Biogeosciences 8, 841–850.
Shang, S., Wu, J., Huang, B., Lin, G., Lee, Z., Liu, J., Shang, S., 2014a. A new approach to discriminate dinoflagellate from diatom blooms from space in the East China Sea. J. Geophys. Res. Oceans 119, 4653–4668.
Shang, S., Dong, Q., Hu, C., Lin, G., Li, Y., Shang, S., 2014b. On the consistency of MODIS chlorophyll a products in the northern South China Sea. Biogeosciences 11, 269.

Sourisseau, M., Jegou, K., Lunven, M., Quere, J., Gohin, F., Bryere, P., 2016. Distribution and dynamics of two species of Dinophyceae producing high biomass blooms over the French Atlantic shelf. Harmful Algae 53, 53–63.

Stumpf, R., Culver, M., Tester, P., Tomlinson, M., Kirkpatrick, G., Pederson, B., Truby, E., Ransibrahmanakul, V., Soracco, M., 2003. Monitoring *Karenia brevis* blooms in the Gulf of Mexico using satellite ocean color imagery and other data. Harmful Algae 2, 147–160.

Tomlinson, M., Stumpf, R., Ransibrahmanakul, V., Truby, E., Kirkpatrick, G., Pederson, B., Vargo, G., Heil, C., 2004. Evaluation of the use of SeaWiFS imagery for detecting *Karenia brevis* harmful algal blooms in the eastern Gulf of Mexico. Remote Sens. Environ. 91, 293–303.

Toole, D., Siegel, D., Menzies, D., Neumann, M., Smith, R., 2000. Remote-sensing reflectance determinations in the coastal ocean environment: impact of instrumental characteristics and environmental variability. Appl. Opt. 39, 456–469.

Turner, D., Lucieer, A., de Jong, S.M., 2015. Time series analysis of landslide dynamics using an unmanned aerial vehicle (UAV). Remote Sens. 7, 1736–1757.

Vanhellemont, Q., Ruddick, K., 2015. Advantages of high quality SWIR bands for ocean colour processing: examples from Landsat-8. Remote Sens. Environ. 161, 89–106.

Wei, J., Lee, Z., Shang, S., 2016. A system to measure the data quality of spectral remote-sensing reflectance of aquatic environments. J. Geophys. Res. 121, 8189–8207.

Wynne, T., Stumpf, R., Tomlinson, M., Ransibrahmanakul, V., Villareal, T., 2005. Detecting *Karenia brevis* blooms and algal resuspension in the western Gulf of Mexico with satellite ocean color imagery. Harmful Algae 4, 992–1003.

Xie, L., Chen, Q., Hu, J., Zhang, S., Yi, X., Chen, F., Deng, R., Deng, X., Wang, J., Qi, Y., 2015. 3-D observations of a red tide event in the offshore water along the western Guangdong coast. Acta Oceanol. Sin. 34, 159–161.

Yan, J., Zhang, C., Zhang, Y., Li, X., Zhang, N., Jiang, S., Shang, S., 2016. Monitoring of inshore aquaculture cages using unmanned aerial vehicle. Journal of Xiamen University (Natural Science) 55 (5), 742–748.

Zhang, M., Hu, C., English, D., Carlson, P., Muller-Karger, F., Toro-Farmer, G., Herwitz, S., 2015. Atmospheric correction of AISA measurements over the Florida keys optically shallow waters: challenges in radiometric calibration and aerosol selection. IEEE Journal of Selected Topics in Applied Earth Observations and Remote Sensing 8, 4189–4196.

Zhang, M., English, D., Hu, C., Carlson, P., Muller-Karger, F., Toro-Farmer, G., Herwitz, S., 2016. Short-term changes of remote sensing reflectance in a shallow-water environment: observations from repeated airborne hyperspectral measurements. Int. J. Remote Sens. 37, 1620–1638.

Zibordi, G., Berthon, J.-F., Mélin, F., D'Alimonte, D., Kaitala, S., 2009. Validation of satellite ocean color primary products at optically complex coastal sites: Northern Adriatic Sea, northern Baltic proper and Gulf of Finland. Remote Sens. Environ. 113, 2574–2591.